Robust Mainlobe Dense False Target Jamming Identification Based on 2D Sparse Recovery

Yunhao Ji [1,a,*], Shan Wei [1,b], and Yaobing Lu [1,c]

[1] Beijing Institute of Radio Measurement, China Aerospace Science and Industry Corp Second Research Institute, Beijing.

[a,*] 201010013409@stu.swmu.edu.cn, [b] wishan@stu.cpu.edu.cn,

[c] 201010012613@stu.swmu.edu.cn

Abstract. Mainlobe dense false target jamming has brought great challenges to current radar detection due to its multi-dimensional flexible modulation capability. To this end, many effective solutions have been proposed in recent years. However, the performance of most existing methods will be largely affected in strong noise environment. In actual scenarios, strong noise environments are unavoidable. To solve this problem, this paper proposes a mainlobe dense false target jamming identification method for strong noise environments based on two-dimensional (2D) sparse recovery. First, the angle and time-delay parameters of the pulse are extracted by 2D sparse recovery. Then, the jamming identification is completed using the space-time joint feature difference within a single pulse repetition interval (PRI). On this basis, we also provide a jamming reconstruction and cancellation scheme for strong jamming environments. Compared with existing methods, the proposed method achieves accurate identification and suppression of jamming within a single PRI by effectively utilizing the spatial information of the source. It exhibits excellent robustness to strong noise and jamming environments. Additionally, it has the advantage of significantly reducing computational costs, thereby increasing overall efficiency and practicality. Numerical simulation experiment results verify the effectiveness of the proposed method.

Keywords: Electronic warfare; array signal processing; interference suppression.

1. Introduction

As is well known, radar jamming and anti-jamming are the relationship between spear and shield, and the two restrict and promote each other [1]–[3]. According to the incident direction of jamming, the radar jamming can be classified into sidelobe jamming and mainlobe jamming. For sidelobe jamming, there are some mature processing methods, such as sidelobe cancellers (SLC) [4]–[6], sidelobe blankers (SLB) [7] and ultralow side-lobe[8], [9].

However, the current countermeasures for mainlobe jamming are not yet mature. Especially when certain forms of jamming are incident from the mainlobe, the target detection will be more difficult. For example, when the digital radio frequency memory (DRFM) operates in full-pulse storage mode, it can densely forward intercepted radar pulse within a single PRI. This is called dense false target jamming. Jamming pulses after time-delay or frequency modulation can produce a large number of false targets similar to the target signal at the radar receiver, and the effects of deceptive jamming and blanket jamming can be presented at the same time. When this kind of jamming is incident from the mainlobe, it is also difficult to distinguish in the angle dimension. Therefore, the mainlobe dense false target jamming poses serious challenges to radar detection, such as increasing the false alarm rate, losing track of real targets, and adding extremely heavy computational burden. For this reason, the researchers today have proposed a series of countermeasures such as pulse diversity [10], [11], blind source separation [12], [13], polarization character [14], [15], and frequency diverse array [16], [17]. Especially, the algorithm of distinguishing real echo and mainlobe jamming based on sparse reconstruction has received extensive attention.

Compared with the traditional algorithms, the sparse reconstruction algorithm im-proves the performance of object detection and angle estimation. Basis tracking (BP) is ap-plied to reconstruct the space-time characteristic of the target echo in [18]. Zhou combined sparse Bayesian (SBL) and

spatial adaptive processing to recover target parameters [19]. Chen applied the joint approximation diagonalization of eigenmatrices (JADE) to separate jamming components, and then used SBL to reconstruct target pulses with high accuracy [20]. In [21], the jamming power is reconstructed by compressive sensing by prior information, and the characteristic oblique projection matrix is constructed to eliminate the jamming component. However, the current algorithms based on sparse recovery exist the following two problems: In practical engineering scenarios, the impact of noise cannot be ignored. It is difficult for existing algorithms to accurately reconstruct target pulses in strong noise. In addition, it is difficult to distinguish mainlobe jamming from real target only at the spatial domain. To obtain the parameter differences between target and jamming at multiple domains, it is usually necessary to reconstruct 2D sparse model. And the mainstream approach is to convert the 2D sparse model into a 1D model through Kron-ecker product, which leads to large amount of computational cost [18].

Aiming at solving the computationally intensive problem of 2D sparse model, Mohimani proposed the smoothed l_0 norm (SL0) algorithm which can be processed in re-al-time [22]; Ghafari extended the algorithm to the 2D case in [23] and state a uniqueness constraint for this class of decomposition; In [24], Zhang studied the off-grid 2D sparse model based on first-order Taylor expansion, and proposed Joint-2D-SL0 to solve the grid mismatch problem. However, the recovery effect of the above methods will be largely impacted in noisy environments.

Aiming at solving the poor robustness of existing sparse recovery algorithms, Bu proposed a robust SL0 algorithm (ReSL0) with one regularization parameter based on SL0 in [25]; Hu proposed a robust joint-block sparse recovery method in [26] which is also ap-plied to MIMO radar imaging and achieves good results, but the regularization parameter needs to be selected according to the noise intensity [23]; Chen discussed an adaptive solution of the regularization parameter in [27] to improve the robustness of sparse solution in noisy environment, but the final regularization parameter sometimes cannot converge to a suitable magnitude. To solve it , Lu proposed a robust co-location MIMO radar target detection method based on the 2D block sparsity of the target in the range-Doppler profile [28], but the method only works in the special case where the dictionary matrix is orthonormal, and the initial value of the regularization parameter needs to be preset.

To conclude, there is still a need for a method that can accurately and quickly per-form sparse decomposition of the 2D model in a noisy environment. Therefore, this paper proposes a 2D robust smoothed l_0 norm algorithm (2D-RSL0) with one adaptive regularization parameter, and applies it to SIMO radar mainlobe dense false target jamming identification. Compared with the traditional methods, the proposed method directly de-composes the 2D sparse model, avoiding the high computational complexity caused by the Kronecker product; through the well-designed regularization parameter update approach, the robustness of the algorithm under strong noise can also be improved. In addition, for scenarios with strong jamming energy, it is difficult to accurately extract the target parameters from the restored angle-time plane. We adapt the least-squares (LS) solution to estimate the jamming intensity to reconstruct jamming pulses. After jamming cancellation, the range unit of the target can be accurately identified on the range profile obtained by pulse compression (PC).

The structure of the paper is organized as follows. In Section II, the array signal model is introduced. Subsequently, in Section III, a mainlobe dense false target jamming identification and suppression method based on 2D sparse recovery is proposed. In addition, the selection of the adaptive regularization parameter and the complexity analysis of the algorithm are discussed in Section III. Numerical simulation experiment results are presented in Section IV. Finally, Section V presents some conclusions and discuss future work.

2. Signal Model

Consider an L element uniform linear array composed of omnidirectional antennas, the distance between the element spacing is d , assuming that there are U narrowband signals

incident on the array in the spatial domain, and the distance between the signal and array satisfies the far field condition, the array receiving samples of the t^{th} snapshot can be expressed as:

$$x(t)=\mathbf{A}s(t)+n(t) \tag{1}$$

where $\mathbf{A}=\left[\mathbf{a}(\theta_1),\mathbf{a}(\theta_2),\cdots,\mathbf{a}(\theta_U)\right]$ represents the array manifold, θ_u represents the incident angle of the u^{th} signal. $\mathbf{a}(\theta_u)=\left[1,e^{j\frac{2\pi d\sin\theta_u}{\lambda}},\cdots,e^{j\frac{2\pi d(L-1)\sin\theta_u}{\lambda}}\right]^{\mathrm{T}}$ is the steering vector of θ_u. $\mathbf{s}(t)$ is the incident signal vector.

Assuming that the radar transmits a linear-frequency modulation (LFM) pulse, the transmitted signal can be expressed as:

$$\mathrm{x(t)=rect}\left(\frac{\mathrm{t}}{\tau}\right)\exp\left(\mathrm{j}\pi\gamma\mathrm{t}^2+\mathrm{j}2\pi\mathrm{f}_0\mathrm{t}\right) \tag{2}$$

where τ is the pulse width, γ is the chirp rate and f_0 is the carrier frequency. And:

$$\mathrm{rect}(t)=\begin{cases}1, & -0.5\le t\le 0.5\\ 0, & \text{others}\end{cases} \tag{3}$$

Suppose the echo signal $s_0(t)$ is from a moving target and has been down-converted, $s_0(t)$ can be expressed as:

$$s_0(t)=A_0\mathrm{rect}\left(\frac{t-t_r}{\tau}\right)\exp\left(j\pi\gamma(t-t_r)^2+j2\pi f_{\mathrm{d}}(t-t_r)\right) \tag{4}$$

where A_0 is the complex amplitude of the target. t_r represents the echo delay, f_{d} is the target's Doppler frequency. γ represents the chirp rate. For brevity, the carrier frequency phase is omitted.

The jammer will continuously emit jamming signals after modulating the r signal, which will cause the echo signal to produce multiple false targets after pulse compression. Without loss of generality, taking time-delay modulation as an example, assuming that there are K jammers around the target. The k^{th} jammer intercepts the radar signal and then modulates the time-delay and produces Q_k jamming pulses. The received jamming signal can be expressed as:

$$s_k(t)=\sum_{q=1}^{Q_k}A_{kq}\mathrm{rect}\left(\frac{t-t_{kq}}{\tau}\right)\exp\left(j\pi\gamma(t-t_{kq})^2+j2\pi f_d(t-t_{kq})\right) \tag{5}$$

where t_{kq} represents the time-delay of the q^{th} jamming pulse forwarded by the k^{th} jammer, and A_{kq} represents the modulation amplitude of the jamming pulse.

For P snapshots from t_1 to t_P, the array model can be obtained in a similar way:

$$\mathbf{X}=\mathbf{AS}+\mathbf{N} \tag{6}$$

where $\mathbf{S}=\begin{bmatrix}s_0(t_1),\cdots,s_0(t_P)\\ \vdots\\ s_K(t_1),\cdots,s_K(t_P)\end{bmatrix}$ and $\mathbf{N}=\left[\mathbf{n}(t_1),\cdots,\mathbf{n}(t_P)\right]$.

It can be seen that the above formula is actually a multiple measurement vectors (MMV) model. We can design dictionary matrices for spatial domain and waveform domain respectively, and perform sparse representation for $\mathbf{A}$ and $\mathbf{S}$ respectively.

Assuming that the source positions of interest are all concentrated in the angle area $\boldsymbol{\Theta}$. By sampling $\boldsymbol{\Theta}$ at equal intervals, the angle sequence $\left[\hat{\theta}_1,\hat{\theta}_2,\cdots,\hat{\theta}_M\right]$ with the number of elements M is obtained, and their steering vectors forms the dictionary matrix in the spatial domain:

$$\mathbf{\Phi}_A = \left(\mathbf{a}\left(\hat{\theta}_1\right), \mathbf{a}\left(\hat{\theta}_2\right), \cdots, \mathbf{a}\left(\hat{\theta}_M\right)\right) \tag{7}$$

According to the prior information, we assume that the echo centers of the target and all jamming pulses are concentrated in $\left[t_{\min}, t_{\max}\right]$, then all echo data samples can be sampled in $\left[t_{\min} - \tau/2, t_{\max} + \tau/2\right]$. The number of sampling snapshots is $f_s\left(t_{\max} - t_{\min} + \tau\right) + 1$, where f_s is the sampling frequency. By sampling $\left[t_{\min}, t_{\max}\right]$ at an interval of Δt, the time-delay sequence $\left[t_1, t_2, \cdots, t_N\right]$ is obtained, where $t_n = t_{\min} + (n-1)\Delta t$. The smaller Δt is, the more accurate the recovery effect is. Choose the function close to the target echo as the atom of waveform domain:

$$s_{\tau n}(t) = \text{rect}\left(\frac{t - t_n}{\tau}\right)\exp\left(j\pi\gamma\left(t - t_n\right)^2 + j2\pi f_d\left(t - t_n\right)\right) \tag{8}$$

where $t \in \left[t_{\min} - \frac{\tau}{2}, t_{\max} + \frac{\tau}{2}\right]$. The Doppler difference between the target and jamming was not considered because the envelope change caused by this difference is very small in a single PRI. Therefore, a slight mismatch in Doppler does not affect the waveform characteristics. All the time-delayed atoms form the dictionary in the waveform domain:

$$\mathbf{\Phi}_S = \left[\mathbf{s}_1, \mathbf{s}_2 \cdots, \mathbf{s}_N\right] \tag{9}$$

where $\mathbf{s}_n = \left[s_{\tau n}(t_1), s_{\tau n}(t_2), \cdots, s_{\tau n}(t_P)\right]$. In this way, $\mathbf{A}$ and $\mathbf{S}$ can be sparsely represented as:

$$\mathbf{A} = \mathbf{\Phi}_A\left[\alpha_1, \alpha_2, \cdots, \alpha_F\right] \tag{10}$$

and

$$\mathbf{S} = \left[\beta_1, \beta_2, \cdots, \beta_F\right]^{\mathrm{T}}\mathbf{\Phi}_S{}^{\mathrm{T}} \tag{11}$$

where $\left[\alpha_1, \alpha_2, \cdots, \alpha_F\right]$ and $\left[\beta_1, \beta_2, \cdots, \beta_F\right]$ represent the coefficient vector of $\mathbf{\Phi}_A$ and $\mathbf{\Phi}_S$ respectively. $F = 1 + \sum_{k=1}^{K} Q_k$ represents the number of received pulses.

Finally, the 2D sparse model of $\mathbf{X}$ can be expressed as:

$$\mathbf{X} = \mathbf{\Phi}_A\left[\alpha_1, \alpha_2, \cdots, \alpha_F\right]\begin{bmatrix}\beta_1^{\mathrm{T}} \\ \beta_2^{\mathrm{T}} \\ \vdots \\ \beta_F^{\mathrm{T}}\end{bmatrix}\mathbf{\Phi}_S{}^{\mathrm{T}} + \mathbf{N} \tag{12}$$

It can be simplified to the following form:

$$\mathbf{X} = \mathbf{\Phi}_1\mathbf{H}\mathbf{\Phi}_2 + \mathbf{N} \tag{13}$$

where $\mathbf{\Phi}_1 = \mathbf{\Phi}_A \in \mathbb{C}^{L\times M}$ and $\mathbf{\Phi}_2 = \mathbf{\Phi}_S{}^{\mathrm{T}} \in \mathbb{C}^{N\times P}$, $\mathbf{H} \in \mathbb{C}^{M\times N}$ is the coefficient matrix. Equation (13) is called the two-dimensional sparse model. Considering that the target and the jamming have only a few strong scattering points in the joint dimension of spatial and time-delay, it is possible to extract target parameters by using 2D sparse recovery.

3. The proposed method

In this section, a 2D robust smoothed l_0 norm based mainlobe repeater jamming identification method is proposed. Especially, an adaptive solution method for the regularization parameter of 2D model is proposed to improve the robustness of the algorithm to noise, thereby enhancing the identification ability of radar to mainlobe repeater jamming in strong noise environment. Subsequently, we proposed a jamming reconstruction and cancellation scheme to avoid the problem of inaccurate target parameter estimation by 2D-RSL0 under strong jamming and strong noise.

3.1 Basic principle of 2D-RSL0

The coefficient matrix $\mathbf{H}$ can be reconstructed by solving the following problem:

$$\begin{cases} \min\limits_{\mathbf{H}} \left\|\mathbf{H}\right\|_F \\ s.t. \left\|\mathbf{X}-\mathbf{\Phi}_1\mathbf{H}\mathbf{\Phi}_2\right\|_F < \varepsilon \end{cases} \tag{14}$$

where $\left\|\cdot\right\|_F$ is the Frobenius norm. ε represents the noise level. However, the regularization of l_0 norm in (14) is an NP-hard problem, which makes it difficult to reconstruct $\mathbf{H}$. As in [23], the discontinuous l_0 norm can be approximated by introducing the Gaussian function family, and the following Gaussian function $G(h)$ can be used to measure the sparsity of the 2D sparse matrix:

$$G(h)=\exp\left(-\frac{h^2}{2\sigma^2}\right) \tag{15}$$

when $\sigma \to 0$, there is $G(h)=\begin{cases}1, h=0\\ 0, h\neq 0\end{cases}$, so for sufficiently small σ:

$$\left\|\mathbf{H}\right\|_{F,0} = MN - \lim_{\sigma\to 0} F_\sigma(\mathbf{H}) \tag{16}$$

where $F_\sigma(\mathbf{H})=\sum\limits_{i=1}^{M}\sum\limits_{j=1}^{N}\exp\left(-\frac{\mathbf{H}_{i,j}{}^2}{2\sigma^2}\right)$.

Therefore, (14) can be transformed into the following optimization problem:

$$\begin{cases} \max\limits_{\mathbf{H}} \lim\limits_{\sigma\to 0} F_\sigma(\mathbf{H}) \\ \text{s.t.} \left\|\mathbf{X}-\mathbf{\Phi}_1\mathbf{H}\mathbf{\Phi}_2\right\|_F < \varepsilon \end{cases} \tag{17}$$

A small σ results in multiple local maxima for $F_\sigma(\mathbf{H})$, which makes it difficult to apply the steepest descent method to find the global optimal solution. Fortunately, $F_\sigma(\mathbf{H})$ will smooth out as σ increases. Therefore, we design a nested loop, and adapt a large value of σ at the beginning of the external loop to avoid the iterative solution from falling into a local optimum . As σ decreases, $F_\sigma(\mathbf{H})$ will more accurately approximate the l_0 norm. The internal loop iterates a small fixed value, which can be described as the following two steps: firstly, iteratively optimizes the solution of the coefficient matrix through the steepest descent algorithm, then projects the solution into the feasible set.

Remark1：In the first step, the iterative form of the steepest descent method is:

$$\hat{\mathbf{H}} \leftarrow \mathbf{H} + \mu_j \nabla F_\sigma(\mathbf{H}) \tag{18}$$

where $\nabla F_\sigma(\mathbf{H})$ is the derivative of $F_\sigma(\mathbf{H})$, which can be expressed as:

$$\nabla F_\sigma(\mathbf{H}) = \left[-\frac{\mathbf{H}_{i,j}}{\sigma^2}\exp\left(-\frac{\mathbf{H}_{i,j}{}^2}{2\sigma^2}\right)\right] \tag{19}$$

The step size μ_j should be proportional to σ^2 [22], we choose a fixed constant μ such that $\mu_j = \mu\sigma^2$.Then the iterative solution can be expressed as:

$$\hat{\mathbf{H}} \leftarrow \mathbf{H} - \mu\left[\mathbf{H}_{i,j}\exp\left(-\frac{\mathbf{H}_{i,j}{}^2}{2\sigma^2}\right)\right] \tag{20}$$

Remark2：The iterative solution $\hat{\mathbf{H}}$ obtained by (20) does not satisfy the constraints of (17), so it needs to be projected into the feasible set, which is equivalent to solve the following optimization problem:

$$\begin{cases} \min\limits_{\mathbf{H}} \left\| \mathbf{H}-\hat{\mathbf{H}} \right\|_F^2 \\ \text{s.t.} \left\| \mathbf{\Phi}_1 \mathbf{H} \mathbf{\Phi}_2 - \mathbf{X} \right\|_F < \varepsilon \end{cases} \tag{21}$$

A common solution to (21) is the Lagrange multiplier method [27], and the Lagrange form of (21) is:

$$J(\mathbf{H}) = \left\| \mathbf{H}-\hat{\mathbf{H}} \right\|_F^2 + \lambda \left\| \mathbf{\Phi}_1 \mathbf{H} \mathbf{\Phi}_2 - \mathbf{X} \right\|_F^2 \tag{22}$$

where λ represents the regularization parameter, it is used to balance the sparsity and residual fitting of $\mathbf{H}$. The selection of λ will be discussed in section 3.2.

The partial derivative of $J(\mathbf{H})$ can be calculated by the following formula:

$$\begin{aligned} \frac{\partial J(\mathbf{H})}{\partial \mathbf{H}} &= \frac{\partial \left[\operatorname{tr}\left(\mathbf{H}-\hat{\mathbf{H}}\right)\left(\mathbf{H}-\hat{\mathbf{H}}\right)^{\mathrm{H}} \right]}{\partial \mathbf{H}} + \lambda \frac{\partial \left[\operatorname{tr}\left(\mathbf{\Phi}_1 \mathbf{H} \mathbf{\Phi}_2 - \mathbf{X}\right)\left(\mathbf{\Phi}_1 \mathbf{H} \mathbf{\Phi}_2 - \mathbf{X}\right)^{\mathrm{H}} \right]}{\partial \mathbf{H}} \\ &= 2\left(\mathbf{H}-\hat{\mathbf{H}}\right) + \lambda \frac{\partial \left[\operatorname{tr}\left(\mathbf{\Phi}_1 \mathbf{H}_1 \mathbf{\Phi}_2 - \mathbf{X}\right)\left(\mathbf{\Phi}_1 \mathbf{H}_2 \mathbf{\Phi}_2 - \mathbf{X}\right)^{\mathrm{H}} \right]}{\partial \mathbf{H}_1} + \lambda \frac{\partial \left[\operatorname{tr}\left(\mathbf{\Phi}_1 \mathbf{H}_1 \mathbf{\Phi}_2 - \mathbf{X}\right)\left(\mathbf{\Phi}_1 \mathbf{H}_2 \mathbf{\Phi}_2 - \mathbf{X}\right)^{\mathbf{H}} \right]}{\partial \mathbf{H}_2} \\ &= 2\left(\mathbf{H}-\hat{\mathbf{H}}\right) + 2\lambda\left(\mathbf{\Phi}_1{}^{\mathrm{H}} \mathbf{\Phi}_1 \mathbf{H} \mathbf{\Phi}_2 \mathbf{\Phi}_2{}^{\mathrm{H}} - \mathbf{\Phi}_1{}^{\mathrm{H}} \mathbf{X} \mathbf{\Phi}_2{}^{\mathrm{H}}\right) \end{aligned} \tag{23}$$

the following properties can be used to simplify the calculation of (23): When calculating the partial derivative of $J(\mathbf{H})$ to $\mathbf{H}$, each occurrence of $\mathbf{H}$ can be regarded as a new variable, and each result can be added.

Let $\frac{\partial J(\mathbf{H})}{\partial \mathbf{H}} = 0$, we have:

$$\mathbf{BH} + \mathbf{HC} = \mathbf{D} \tag{24}$$

where $\mathbf{B} = \left[\lambda \mathbf{\Phi}_1{}^{\mathrm{H}} \mathbf{\Phi}_1 \right]^{\dagger}$, $\mathbf{C} = \mathbf{\Phi}_2 \mathbf{\Phi}_2{}^{\mathrm{H}}$ and $\mathbf{D} = \left[\lambda \mathbf{\Phi}_1{}^{\mathrm{H}} \mathbf{\Phi}_1 \right]^{\dagger} \left[\hat{\mathbf{H}} + \lambda \mathbf{\Phi}_1{}^{\mathrm{H}} \mathbf{X} \mathbf{\Phi}_2{}^{\mathrm{H}} \right]$. $(\bullet)^{\dagger}$ represents the pseudo-inverse of the matrix.

Equation (24) is the Sylvester equation [29], and the analytical solution of (24) can be obtained by the following formula:

$$\operatorname{vec}(\mathbf{H}) = \left(\mathbf{I}_N \otimes \mathbf{B} + \mathbf{C}^{\mathrm{T}} \otimes \mathbf{I}_M \right) \operatorname{vec}(\mathbf{D}) \tag{25}$$

Bartels and Stewart proposed a fast solution to (24), and gave the restriction that (24) has a unique solution [30].

3.2 Adaptive Selection of Regularization Parameter λ

The update of regularization parameter λ directly affects the performance of 2D-RSL0. In this section, we design an adaptive iterative method for the update of λ. By introducing the regularization parameter λ, 2D-RSL0 obtains stronger robustness than 2D-SL0. It can be seen from (22) that the former term of $J(\mathbf{H})$ is used to control the approximation of the solution to the steepest descent solution, aiming to ensure the sparsity of the result. The latter term is the regularization term that minimizes the residual. Therefore, an ideal λ should balance the sparsity and robustness of the solution, let $\frac{\partial J(\mathbf{H})}{\partial \mathbf{H}} = 0$, we have:

$$\left(\mathbf{H}-\hat{\mathbf{H}}\right) = -\lambda\left(\mathbf{\Phi}_1{}^{\mathrm{H}} \mathbf{\Phi}_1 \mathbf{H} \mathbf{\Phi}_2 \mathbf{\Phi}_2{}^{\mathrm{H}} - \mathbf{\Phi}_1{}^{\mathrm{H}} \mathbf{X} \mathbf{\Phi}_2{}^{\mathrm{H}}\right) \tag{26}$$

Taking the Frobenius norm on both sides of (26), then it should satisfy:

$$\lambda = \frac{\left\| \left(\mathbf{H}-\hat{\mathbf{H}}\right) \right\|_F}{\left\| \mathbf{\Phi}_1{}^{\mathrm{H}} \mathbf{\Phi}_1 \mathbf{H} \mathbf{\Phi}_2 \mathbf{\Phi}_2{}^{\mathrm{H}} - \mathbf{\Phi}_1{}^{\mathrm{H}} \mathbf{X} \mathbf{\Phi}_2{}^{\mathrm{H}} \right\|_F} \tag{27}$$

The projected solution $\mathbf{H}$ in (27) is an unknown prior. The projected solution $\mathbf{H}_{j-1}$ of the $j-1^{th}$ loop is chosen as its replacement in [27], then λ can be estimated by:

$$\hat{\lambda}_j = \frac{\left\| \left(\mathbf{H}_{j-1} - \hat{\mathbf{H}} \right) \right\|_F}{\left\| \mathbf{\Phi}_1^{\mathrm{H}} \mathbf{\Phi}_1 \mathbf{H}_{j-1} \mathbf{\Phi}_2 \mathbf{\Phi}_2^{\mathrm{H}} - \mathbf{\Phi}_1^{\mathrm{H}} \mathbf{X} \mathbf{\Phi}_2^{\mathrm{H}} \right\|_F} \tag{28}$$

However, it will bring the following two problems:

1. In general, large λ corresponds to small σ [25]. σ is a large value under strong noise. For the initial solution $\mathbf{H}_0$, the minimum norm solution with $\mathbf{X} = \mathbf{\Phi}_1 \mathbf{H} \mathbf{\Phi}_2$ is generally selected as the initial solution, which causes the denominator of (28) to be a very small value, resulting in the initial solution $\hat{\lambda}_1$ being too large.

2. Since the projection solution $\mathbf{H}_{j-1}$ of the $j-1^{\text{th}}$ external loop satisfies the following equation:

$$\left(\mathbf{H}_{j-1} - \hat{\mathbf{H}}_{j-1} \right) + \hat{\lambda}_{j-1} \left(\mathbf{\Phi}_1^{\mathrm{H}} \mathbf{\Phi}_1 \mathbf{H}_{j-1} \mathbf{\Phi}_2 \mathbf{\Phi}_2^{\mathrm{H}} - \mathbf{\Phi}_1^{\mathrm{H}} \mathbf{X} \mathbf{\Phi}_2^{\mathrm{H}} \right) = 0 \tag{29}$$

Equation (28) can be simplified to $\hat{\lambda}_j = u_{j-1} \hat{\lambda}_{j-1}$, where u_{j-1} is the iteration factor, and it can be expressed as:

$$u_{j-1} = \frac{\left\| \left(\hat{\mathbf{H}} - \mathbf{H}_{j-1} \right) \right\|_F}{\left\| \left(\mathbf{H}_{j-1} - \hat{\mathbf{H}}_{j-1} \right) \right\|_F} \tag{30}$$

where $\left(\hat{\mathbf{H}} - \mathbf{H}_{j-1} \right)$ represents the variation of the gradient solution in the j^{th} external loop, $\left(\mathbf{H}_{j-1} - \hat{\mathbf{H}}_{j-1} \right)$ represents the variation of the projection solution in the $j-1^{\text{th}}$ external loop. It can be seen that $\hat{\lambda}$ is not strictly decreasing.

The above two points make it difficult for $\hat{\lambda}$ to converge to an appropriate order of magnitude. Therefore, we give the following iterative formula:

$$\hat{\lambda}_j = \frac{\left\| \left(\mathbf{H}_{j-1} - \hat{\mathbf{H}} \right) \right\|_F}{\left\| \mathbf{\Phi}_1^{\mathrm{H}} \mathbf{\Phi}_1 \hat{\mathbf{H}} \mathbf{\Phi}_2 \mathbf{\Phi}_2^{\mathrm{H}} - \mathbf{\Phi}_1^{\mathrm{H}} \mathbf{X} \mathbf{\Phi}_2^{\mathrm{H}} \right\|_F} \tag{31}$$

by replacing $\mathbf{H}_{j-1}$ in the denominator with $\hat{\mathbf{H}}$, the problem of too large initial solution is solved. Compared with $\mathbf{H}_{j-1}$, the new expression contains the gradient information of this loop, which is closer to the estimated value of $\mathbf{H}$. Therefore, the new $\hat{\lambda}_j$ is more accurate than the traditional method.

3.3 Overall flowchart of 2D-RSL0

Finally, we propose the 2D-RSL0 algorithm with the adaptive iterative method for the update of λ, the flowchart is shown in Algorithm 1. By designing two nested loops, σ is continuously reduced in the external loop, and the residual error of $F_\sigma(\mathbf{H})$ fitting the l_0 norm is reduced. In the internal loop, calculate the optimal solution that satisfies the constraints under the current σ with a fixed number of iterations. Such a structure can quickly obtain an approximate solution to the optimal solution in the early stage of the external loop, and the final sparse solution $\mathbf{H}$ can effectively avoid many local optimal solutions when σ is small.

Algorithm 1 The Two-Dimensional Robust SL0 Algorithm (2D-RSL0)

Input: Received data $\mathbf{X}$; Dictionary $\mathbf{\Phi}_1, \mathbf{\Phi}_2$.
Output: Recovered time-delay matrix $\mathbf{H}$.

Initialization
Let $\mathbf{H}_0 = \mathbf{\Phi}_1^{\dagger}\mathbf{X}\left(\mathbf{\Phi}_2{}^{\mathrm{T}}\mathbf{\Phi}_2\right)^{-1}\mathbf{\Phi}_2{}^{\mathrm{T}}$.
Select an appropriate descending sequence for σ, $\left[\sigma_1,\sigma_2,\ldots,\sigma_J\right]$.
for $j=1,2,\ldots,J$
  Let $\sigma=\sigma_j$.
  Let $\mathbf{H}=\mathbf{H}_{j-1}$
  for $g=1,2,\ldots,G$
    Update regularization parameter $\hat{\lambda}$:
    if $g=1$ then
      Calculate $\hat{\lambda}$ by (31)
    end if
    Maximize $F_\sigma(\mathbf{H})$ using the steepest ascent algorithm:
    Calculate $\nabla F_\sigma(\mathbf{H})$ by (19)
    Calculate $\hat{\mathbf{H}}=\mathbf{H}+\mu\sigma^2\nabla F_\sigma(\mathbf{H})$
    Project $\hat{\mathbf{H}}$ back onto the feasible set $\left\|\mathbf{\Phi}_1\mathbf{H}\mathbf{\Phi}_2-\mathbf{X}\right\|_F<\varepsilon$:
    Using Bartels–Stewart algorithm to calculate $\mathbf{H}$ by (24)
  end for
  Set $\mathbf{H}_j=\mathbf{H}$
end for
$\mathbf{H}=\mathbf{H}_J$
return $\mathbf{H}$

3.4 Complexity Analysis of 2D-RSL0

The calculation load of 2D-RSL0 is mainly concentrated on the step of calculating the projection solution through (24). The complexity of $\left[\lambda\mathbf{\Phi}_1{}^{\mathrm{H}}\mathbf{\Phi}_1\right]^{\dagger}$ is $O\left(M^2L+3M^3\right)$, the complexity of $\mathbf{\Phi}_2\mathbf{\Phi}_2{}^{\mathrm{H}}$ is $O\left(N^2P\right)$. The previous term of $\left[\lambda\mathbf{\Phi}_1{}^{\mathrm{H}}\mathbf{\Phi}_1\right]^{\dagger}\left[\hat{\mathbf{H}}+\lambda\mathbf{\Phi}_1{}^{\mathrm{H}}\mathbf{X}\mathbf{\Phi}_2{}^{\mathrm{H}}\right]$ can be obtained when calculating $\mathbf{B}$, so the complexity can be reduced to $O\left(M^3+M^2L+M^2P\right)$. Using the Bartels-Stewart algorithm, the complexity of solving the Sylwester equation can be reduced from $O\left(M^3N^3\right)$ to $O\left(10M^3+10N^3+2.5M^2N+\ 2.5MN^2\right)$. For the nested loop given in Algorithm 1, it is necessary to solve the Sylwester equation JL times. Therefore, the total complexity of the projection step is $O\left(14M^3JG+10N^3JG+2M^2LJG+M^2PJG+N^2PJG+2.5M^2NJG+2.5MN^2JG\right)$. $\left[\mathbf{\Phi}_1{}^{\mathrm{H}}\mathbf{\Phi}_1\right]^{\dagger}$ and $\mathbf{\Phi}_2\mathbf{\Phi}_2{}^{\mathrm{H}}$ can be precomputed outside the loop, o the total complexity can be reduced to $O\left(11M^3JG+10N^3JG+2.5M^2NJG+M^2LJG+M^2PJG+2.5MN^2JG+M^2L+3M^3+N^2P\right)$.

For comparison, RKSL0 is introduced here. By the Kronecker product and the random projection matrix, (13) can also be transformed into a 1D sparse model and solved by ReSL0 [27], which is called the RKSL0 method. Assuming that the random projection matrix has W rows, then the total complexity of RKSL0 is $O\left(2W^2MNJG+W^3JG+2WMNJG\right)$. It can be seen that the complexity of the proposed algorithm is significantly lower than that of RK-SL0. This is mainly because in order to ensure the uniqueness of the sparse solution, the row dimension of the random projection matrix must satisfy $W>F\log LP$, which makes the complexity of RK-SL0 greatly improves.

3.5 Jamming Reconstruction and Cancellation

The dense and strong jamming will cause the real target intensity recovered on the angle-time plane to be weak, which brings difficulties to the parameter estimation of the real target and seriously affects the detection and tracking of the real target. However, the recovered jamming parameters by 2D-RSL0 can be used to reconstruct the jamming pulses to cancel jamming Assuming that there are W identified jamming pulses on the angle-time plane, in which the steering vector and the waveform of the $w-th$ jamming can be constructed as $\mathbf{a}^w$ and $\mathbf{s}^w$ respectively. Then, the constructed jamming data can be expressed as:

$$\mathbf{X}_J = \sum_{w=1}^{W} r^w \mathbf{a}^w \left(\mathbf{s}^w\right)^{\mathrm{T}} \tag{32}$$

where r^w represents the intensity of the $w-th$ jamming pulse, and the unknown jamming intensity vector can be defined as $\boldsymbol{\gamma} = \left[r^1, r^2, \ldots, r^W\right]$. It can be estimated by solving the following least-squares problem:

$$\begin{aligned} \boldsymbol{\gamma} &= \arg\min_{\boldsymbol{\gamma}} \left\| \mathbf{X} - \mathbf{X}_J \right\|_F \\ &= \arg\min_{\boldsymbol{\gamma}} \left\| vec\left(\mathbf{X} - \sum_{w=1}^{W} r^w \mathbf{a}^w \left(\mathbf{s}^w\right)^{\mathrm{T}} \right) \right\|_2 \\ &= \arg\min_{\boldsymbol{\gamma}} \left\| vec\left(\mathbf{X}\right) - \boldsymbol{\Lambda}\boldsymbol{\gamma} \right\|_2 \end{aligned} \tag{33}$$

where $\boldsymbol{\Lambda} = \left[vec\left(\mathbf{a}^1\left(\mathbf{s}^1\right)^{\mathrm{T}}\right), vec\left(\mathbf{a}^2\left(\mathbf{s}^2\right)^{\mathrm{T}}\right) \ldots, vec\left(\mathbf{a}^W\left(\mathbf{s}^W\right)^{\mathrm{T}}\right) \right]$. $\|\cdot\|_2$ represents the Euclidean norm. Therefore, the jamming intensity vector $\boldsymbol{\gamma}$ can be estimated as:

$$\boldsymbol{\gamma} = \left(\boldsymbol{\Lambda}^{\mathrm{H}}\boldsymbol{\Lambda}\right)^{-1} \boldsymbol{\Lambda} vec\left(\mathbf{X}\right) \tag{34}$$

On this basis all jamming pulses can be reconstructed. After jamming cancellation, the remaining data $\mathbf{X}_{out}$ can be expressed as:

$$\mathbf{X}_{out} = \mathbf{X} - \sum_{w=1}^{W} r^w \mathbf{a}^w \left(\mathbf{s}^w\right)^{\mathrm{T}} \tag{35}$$

Finally, the range unit of the real target can be solved by traditional adaptive beam forming (DBF) and PC. It should be noted that since the mainlobe jamming has been canceled, although the target angle estimated by 2D-RSL0 is not accurate enough, the MVDR or LCMV beamformer can still be designed based on the estimated target angle to process $\mathbf{X}_{out}$.

4. Experiments

Consider a uniform line array with 32 omni-directional antennas. The array element spacing d is half the wavelength l_{w}, and the 3dB beamwidth is $\theta_{BW} = 50.7 l_{\mathrm{w}} / Ld = 3.1688°$. The radar transmits LFM signal with the bandwidth $B = 5\mathrm{MHz}$ and the pulse width $\tau = 20\mu\mathrm{s}$. The sampling frequency is $f_{\mathrm{s}} = 10\mathrm{MHz}$, and the chirp rate is $\gamma = B/\tau$. Assuming there is a moving target 30km away from the radar in the direction of $0°$, and the target speed is $300\mathrm{m/s}$. Three jamming scenarios are considered, and the corresponding parameters are shown in Table 1, Table 2 and Table 3 respectively. Assume that the direction of target is not known in advance, $\theta_{\min}$ and $\theta_{\max}$ are chosen as $-10°$ and $10°$. The angular interval is $\Delta\theta = 0.1°$, so the number of atoms in the spatial domain dictionary is $M = \left(\theta_{\max} - \theta_{\min}\right)/\Delta\theta + 1$. Similarly, $t_{\min}$ and $t_{\max}$ are chosen as $0.2\mathrm{ms}$ and $0.22\mathrm{ms}$. The time-delay interval is $\Delta t = 0.2\mu\mathrm{s}$, so the number of atoms in the

time-delay domain dictionary is $N=\left(t_{\max}-t_{\min}\right)/\Delta t+1$. The input parameters of 2D-RSL0 method are $\sigma_{\min}=0.01$, $J=100$, $\mu=0.2$, $G=3$ respectively. The parameter decay rate of σ is set to 0.5.

4.1 Verification experiment in strong noise and jamming

In this section, we verify the effectiveness of the proposed method in strong noise and jamming. The signal-noise-ratio (SNR) is set to -20dB. Fig. 1(a) shows the simulation of scenario 1. Fig. 1(b) shows the simulation of the received echo after pulse compression. It can be seen that in the case of $\text{SNR}=-20\text{dB}$, the signal is still covered by noise after pulse compression, and it is difficult to distinguish the target and jamming from numerous peaks.

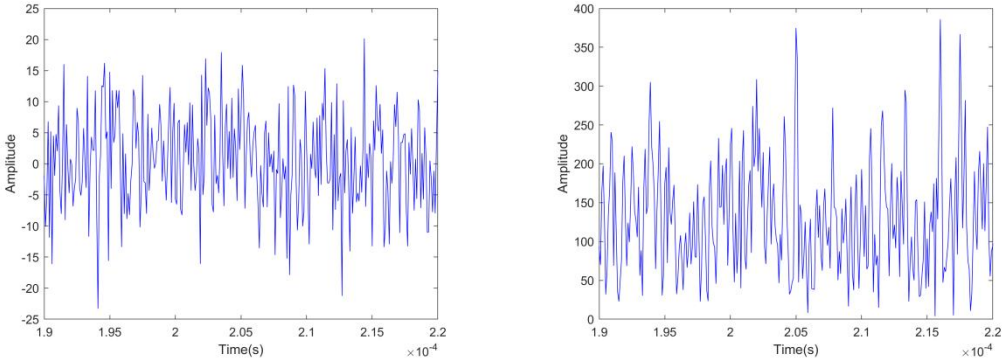

(a) (b)

Fig. 1 (a) Received echo under noise (b) Received echo after pulse compression

In order to distinguish the target and jamming in scenario 1, we adapted 2D-SL0 to reconstruct the pulse parameters in strong noise environment. Fig. 2 shows the recovery results on the angle-time plane and their projections on the two planes. It can be seen that the target and jamming can be effectively identified according to the 2D information. The number of recovered pulses is $K=7$. The angle-time parameter of the pulses are $[1.2°, 0.200\text{ms}]$, $[1.2°, 0.204\text{ms}]$, $[1.2°, 0.207\text{ms}]$, $[1.2°, 0.210\text{ms}]$, $[1.2°, 0.213\text{ms}]$, $[1.2°, 0.216\text{ms}]$ and $[1.2°, 0.219\text{ms}]$ respectively. Since the jamming pulses emitted by the same jammer have the same angle, we can distinguish the target from jammer in this way. From Fig. 2, it can be easily and clearly determined that the target's incident angle is $0°$. And six jamming pulses from the same jammer incident from $1.2°$ can be identified. It should be emphasized that the target direction is not the direction of the first pulse received in the time domain, it is determined by the direction of only one pulse. The angle and time-delay information of the pulse should be referenced simultaneously to determine the true target pulse.

Table 1. Parameter Settings of Scenario 1

Type		Angle(°)	Time-delay(μs)	JSR(dB)
Jammer 1	Pulse 1	1.2	4	3
	Pulse 2	1.2	7	3
	Pulse 3	1.2	10	3
	Pulse 4	1.2	13	3
	Pulse 5	1.2	16	3
	Pulse 6	1.2	19	3

Table 2. Parameter Settings of Scenario 2

Type		Angle(°)	Time-delay(μs)	JSR(dB)
Jammer 1	Pulse 1	-1	10	3
	Pulse 2	-1	13	3
	Pulse 1	-1	16	3

Jammer 2	Pulse 2	1	1	3
	Pulse 1	1	3	3
	Pulse 2	1	5	3

Table 3. Parameter Settings of Scenario 3

Type		Angle(°)	Time-delay(μs)	JSR(dB)
Jammer 1	Pulse 1	-1	10	15
	Pulse 2	-1	13	15
	Pulse 1	-1	16	15
Jammer 2	Pulse 2	1	1	15
	Pulse 1	1	3	15
	Pulse 2	1	5	15

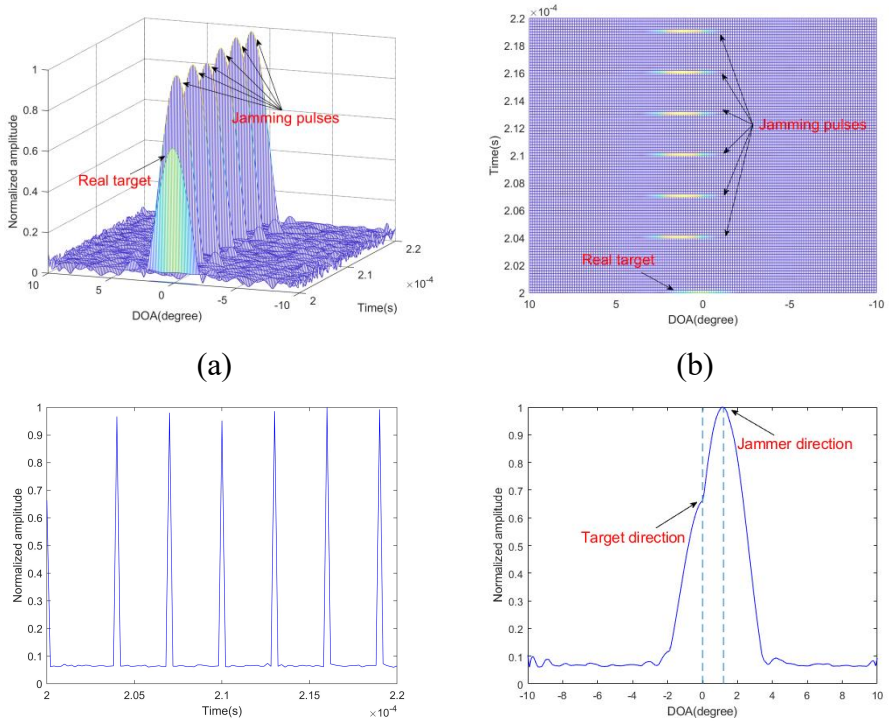

Fig. 2 Recovery results of scenario 1: (a) Angle-time recovery of pulses (b) Top view (c) Time plane projection (d) Angle plane projection

Fig. 3 shows the corresponding experimental results of scenario 2. In this scenario, the angle plane projection shows that the target is covered by the jamming, but the target and the jamming are separable in the time plane projection, so that the target and the jamming can be effectively identified. On the sparse recovery plane of a single PRI, the true target appears only as a single peak that is independent and not modulated by time delay. In contrast, the number of jamming peaks is equal to the number of false targets generated by the two jammers, and all of these false target peaks are located behind the real targets. It is worth noting that all false target peaks generated by the same jammer have the same angle parameters. This layout clearly differentiates between real targets and false targets created by jammers. The distinguishing feature of the real target is that it is a single peak, while the false targets can be identified by their consistent angular parameters and posterior position relative to the real target. The target is incident from $0°$. $[-1°, 0.210\text{ms}]$, $[-1°, 0.213\text{ms}]$ and $[-1°, 0.216\text{ms}]$ are the three pulses emitted by jammer 1, $[1°, 0.201\text{ms}]$, $[1°, 0.203\text{ms}]$ and $[1°, 0.205\text{ms}]$ are the three pulses emitted by jammer 2.

In Fig.4, we analyze the effect of two-dimensional sparse recovery and jamming cancellation in strong jamming scenarios. It can be observed from Fig.4a and Fig.4b that when the jamming is too strong, the representation of the target on the plane appears very weak. In this case, the parameter estimates of the target are often imprecise. However, the parameter estimation of the jamming signal still maintains a high accuracy, so the jamming waveform can be reliably reconstructed. In 4c, based

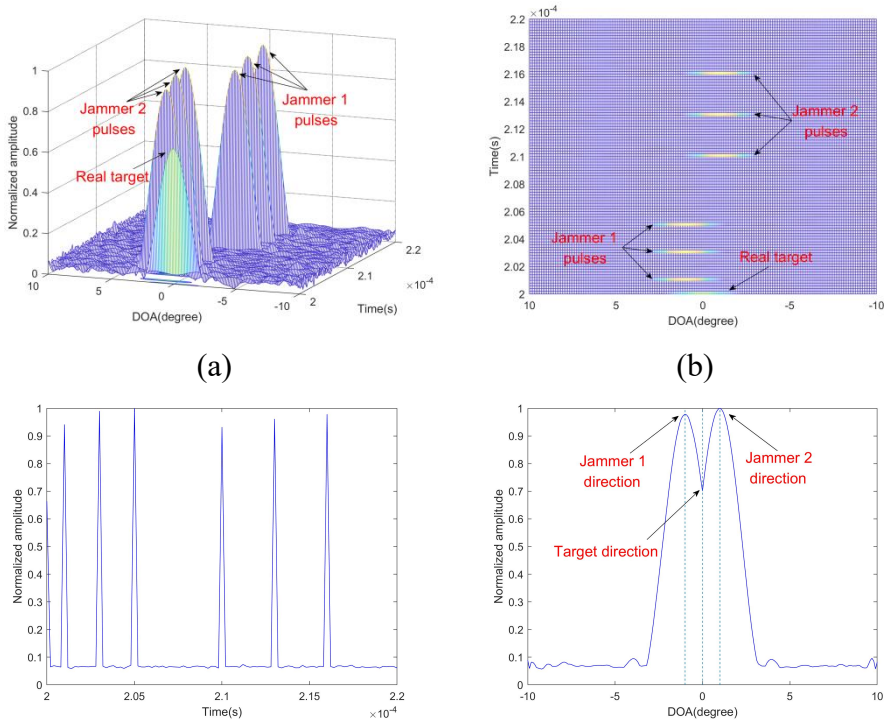

(a) (b)

(c) (d)

Fig. 3 Recovery results of scenario 2: (a) Angle-time recovery of pulses (b) Top view (c) Time plane projection (d) Angle plane projection

on the estimated jamming parameters, the jamming signal is accurately reconstructed and effectively eliminated. After eliminating jamming, the peak profile of the target becomes clearly discernible on the two-dimensional plane. Although there may still be certain errors in the parameter estimation of the target at this time, the pulse compression results after jamming elimination in Fig.4d can be referred to assist in judging the real target and further determine the two-dimensional parameters of the target. The jamming data is reconstructed using the restored jamming parameters.

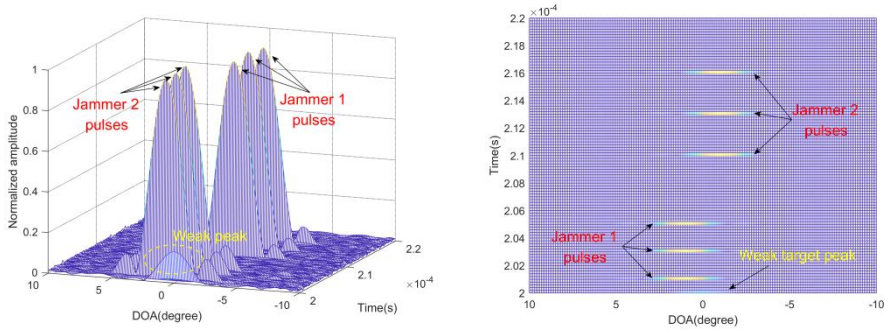

(a) (b)

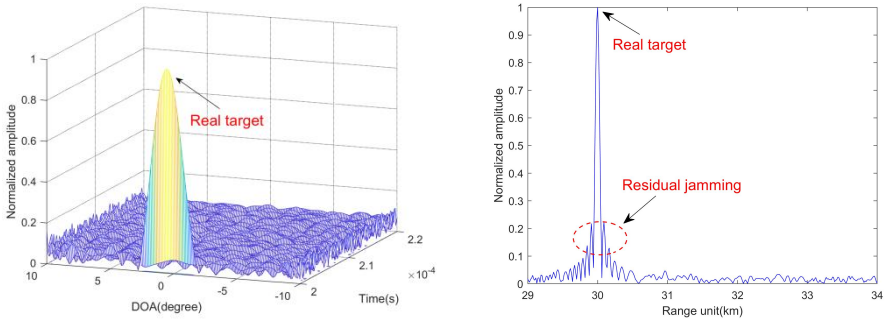

(c) (d)

Fig. 4 Recovery results of scenario 3: (a) Angle-time recovery of pulses (b) Top view (c) Angle-time recovery after jamming cancellation (d) Pulse compression profile after jamming cancellation

4.2 Performance analysis of proposed 2D-RSL0

In this section, we compare the performance of the proposed 2D-RSL0 with RKBP [18] and RKSL0.

4.2.1 Performance comparison under different SNR

Fig. 5 shows the angle-time plane recovery results of the three methods under different SNR. It can be seen that when the noise intensity is low, all methods can effectively reconstruct the pulse parameters and distinguish the target from the jammer. And the pulse normalized amplitude reconstructed by the proposed method is more accurate than RKBP and RMSL0. However, in the case of $\mathrm{SNR} < 0\mathrm{dB}$, the performance of RKBP and RKSL0 decreases rapidly. Many spurious peaks are produced in the reconstruction results, which seriously affect the discrimination of the target and jamming. This is mainly because the random projection changes the intensity of the noise. The proposed method can effectively reconstruct pulse parameters under all four noise intensities, especially when $\mathrm{SNR} = -20\mathrm{dB}$, the proposed method can still accurately reconstruct the pulse parameters which proves that the robustness of the proposed method to noise. The performance improvement of the proposed method is thanks to the consideration of 2D sparsity and the adaptive regularization method in the iterations.

4.2.2 Analysis of the impact of low SNR using RMSE

In Fig. 6, we give the comparison of the three methods' RMSE versus SNR, where RMSE is defined as:

$$\mathrm{RMSE} = \sqrt{\frac{1}{KT_{MC}} \sum_{t=1}^{T_{MC}} \sum_{k=1}^{1} \left(\tilde{\theta}_{tk} - \theta_k \right)^2} \tag{36}$$

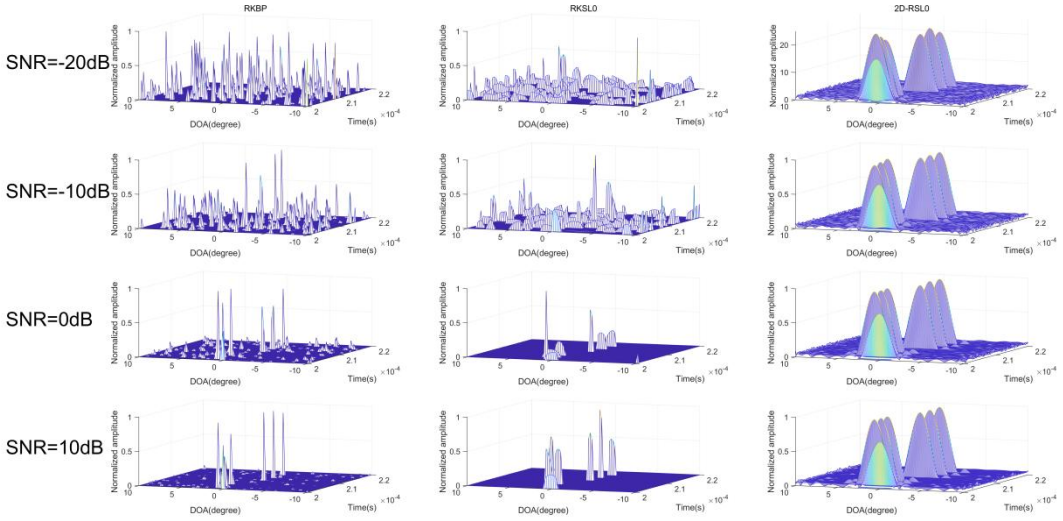

Fig. 5 Comparison of angle-time recovery results under different SNR

where $\tilde{\theta}_{tk}$ represents the DOA estimation of the t^{th} Monte Carlo experiment on the k^{th} pulse, and θ_k is the real angle of the k^{th} pulse. Carry out $T_{MC}=100$ Monte Carlo experiments. It can be seen that the three methods can effectively distinguish the target and jamming when $\mathrm{SNR}>5\mathrm{dB}$. The RMSE of the three methods decreases as the SNR increases, and the proposed method's RMSE is significantly lower than RKBP and RKSL0 when $\mathrm{SNR}=-20\mathrm{dB}$, which means higher accurate parameter estimation accuracy. This is mainly because the introduction of the projection matrix reduces the robustness of RKBP and RKSL0.

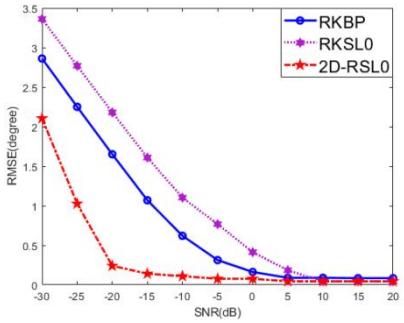

Fig. 6 RMSE versus SNR

4.2.3 Analysis of the impact of the angle between target and jamming using RMSE

In Fig. 7 we analyze the impact of angle between target and jamming using RMSE. It can be seen that the RMSE increases as the angle decreases, which means that the angle estimation of the pulse deviates farther from the true value. When the pulse angle interval is 0.3°, which is one-tenth of the 3dB beamwidth, the RMSE of the proposed method is reduced to within 0.1°, which verifies the high-precision angle estimation capability of the proposed method.

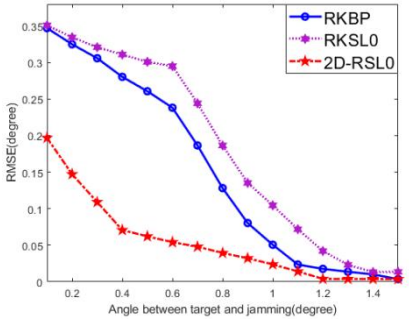

Fig. 7 RMSE versus angle interval

4.2.4 Analysis of the impact of J using RMSE

In order to study the impact of the number of external loops J on the reconstruction performance, we set J as 25, 50, 75, 100, 125, and 150 respectively. Fig. 8 shows the results under different values of J. It can be seen that with the increase of J, the RMSE of the proposed method gradually decreases, but when J increases to a certain level, the estimation accuracy basically remains the same. A higher value of J brings more computational cost. Therefore, in practical applications, the appropriate value of J should strike a balance between computational complexity and reconstruction accuracy.

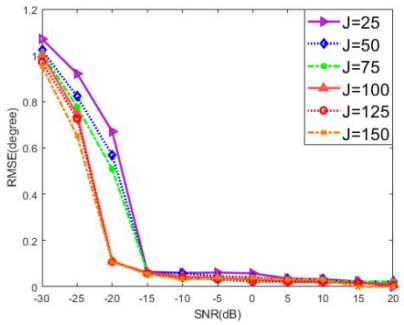

Fig. 8 RMSE versus numbers of external loops J

4.2.5 Analysis of the impact of dictionary atom number using CPU cost time

Fig.9 shows the effect of dictionary atom number using CPU cost time. We set the number of atoms in the angle dictionary and time-delay dictionary to be the same, varying from 50 to 100, and the CPU cost time of the proposed method is significantly shorter than that of RKBP and RKSL0. This is because the two methods straighten two-dimensional data into one-dimensional vector processing, which significantly increases the dimen-sionality of the sample. Although it is possible to reduce the dimensionality of the vector in the way of random projection matrix to reduce the operation cost. However, this reduc-es the robustness of RKBP and RKSL0 to noise, and in order to ensure the stability of sparse solutions, there is a lower limit to the dimensionality reduction of the data.

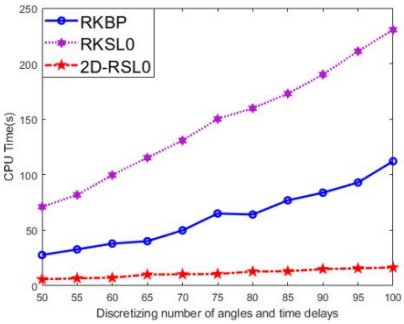

Fig. 9 CPU time versus dictionary atoms

4.3 Performance analysis of target detection

In this section, we analyze the performance of the target detection. Through 100 Monte Carlo experiments, Figure 10 shows the detection probability of Scenario 1 and Scenario 2 under different SNR and jamming-signal-ratio (JSR). It can be seen that when $\mathrm{SNR} \geq -20\mathrm{dB}$, the target detection probabilities in both scenarios are higher than 90%, and the proposed method performs well under the influence of different jamming intensities. When $\mathrm{SNR} < -20\mathrm{dB}$, the target detection probabilities in both scenarios declined to a certain extent. Too strong noise affects the accurate extraction of jamming parameters, resulting in inaccurate calculation of jamming intensity. Therefore, the residual jamming cannot be ignored. Taken together, the detection probability is

relatively the highest when $JSR = 12dB$, which indicates that the residual jamming energy is relatively the lowest. In addition, since the jamming distribution of scenario 2 is more complex than that of scenario 1, the recovered jamming parameters are more inaccurate, and the corresponding target detection probability is also slightly lower.

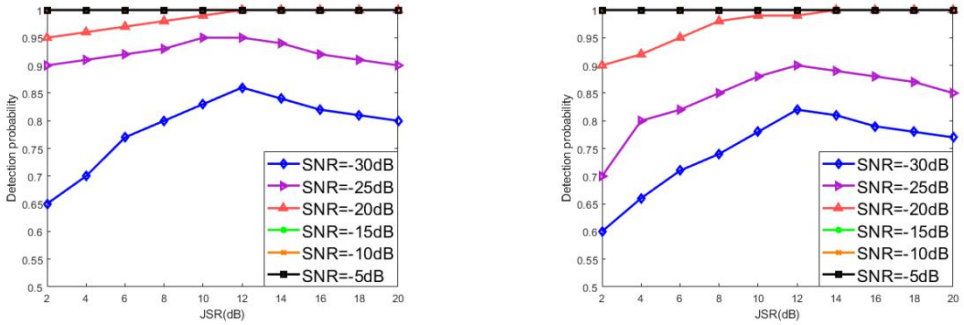

(a) (b)

Fig. 10 Detection probability versus JSR: (a) Scenario 1 (b) Scenario2

5. Conclusion

This paper addresses the issue of insufficient robustness and high computational complexity in the existing mainlobe dense false target jamming identification method under strong noise and jamming background. Compared with the existing methods, by introducing a regularization parameter to adaptively adjust the sparse solution, the proposed method is robust to strong noise environment. Through jamming reconstruction and cancellation based on LS, the proposed method is robust to strong jamming environment. What's more, the method significantly reduces the computational cost by directly decomposing the 2D sparse model. Experiment results show that the proposed method is superior to RKBP and RKSL0 in both accuracy and calculation speed. In addition, even in the case of $SNR = -20dB$ and $JSR = 20dB$, the proposed method can accurately identify the mainlobe dense false target jamming and extract the real target range unit. It is worth mentioning that when DRFM performs time-delay modulation and frequency modulation on the mainlobe jamming pulse at the same time, it is difficult for this method to estimate more than two pulse parameters, which will be the focus of future research.

References

[1] Neng-Jing, L. & Yi-Ting, Z. 1995. A survey of radar ECM and ECCM. *IEEE Transactions on Aerospace and Electronic Systems,* 31**,** 1110-1120. doi: 10.1109/7.395232.

[2] Feng, D., Xu, L., Pan, X. & Wang, X. 2017. Jamming wideband radar using interrupted-sampling repeater. *IEEE Transactions on Aerospace and Electronic Systems,* 53**,** 1341-1354. doi: 10.1109/TAES.2017.2670958.

[3] Lan, L., Xu, J., Liao, G., Zhang, Y., Fioranelli, F. & So, H. C. 2020. Suppression of mainbeam deceptive jammer with FDA-MIMO radar. *IEEE Transactions on Vehicular Technology,* 69**,** 11584-11598. doi: 10.1109/TVT.2020.3014689.

[4] Mohammed, J. R. & Sayidmarie, K. H. 2017. Performance evaluation of the adaptive sidelobe canceller system with various auxiliary configurations. *AEU-International Journal of Electronics and Communications,* 80**,** 179-185. doi: 10.1016/j.aeue.2017.06.039.

[5] Hashimoto, T., Nishimura, K. & Sato, T. 2016. Adaptive sidelobe cancellation technique for atmospheric radars containing arrays with nonuniform gain. *IEICE Transactions on Communications,* 99**,** 2583-2591. doi: 10.1587/transcom.2016EBP3047.

[6] Zhao, X., He, Z., Wang, Y. & Sun, G. 2018. Reduced-dimension STAP using a modified generalised sidelobe canceller for collocated MIMO radars. *IET Radar, Sonar & Navigation,* 12**,** 1476-1483. doi: 10.1049/iet-rsn.2018.5239.

[7] Narasimhan, R., Vengadarajan, A. & Ramakrishnan, K. Mitigation of sidelobe clutter discrete using sidelobe blanking technique in airborne radars. 2018 IEEE Aerospace Conference, 2018. IEEE, 1-12. doi: 10.1109/AERO.2018.8396403.

[8] Keizer, W. P. 2018. Planar phased-array antennas: Mutual coupling and ultralow peak sidelobes. *IEEE Antennas and Propagation Magazine,* 61**,** 14-28. doi: 10.1109/MAP.2018.2883024.

[9] Mohammed, J. 2013. Phased array antenna with ultra-low sidelobes. *Electronics Letters,* 49**,** 1055-1056. doi: 10.1049/el.2013.1642.

[10] Li, S., Zhang, L., Liu, N., Zhang, J. & Zhao, S. 2017. Adaptive detection with conic rejection to suppress deceptive jamming for frequency diverse MIMO radar. *Digital signal processing,* 69**,** 32-40. doi: 10.1016/j.dsp.2017.06.008.

[11] Akhtar, J. & Olsen, K. E. Frequency agility radar with overlapping pulses and sparse reconstruction. 2018 IEEE Radar Conference (RadarConf18), 2018. IEEE, 0061-0066. doi: 10.1109/RADAR.2018.8378531.

[12] Ge, M., Cui, G., Yu, X. & Kong, L. 2020. Main lobe jamming suppression via blind source separation sparse signal recovery with subarray configuration. *IET radar, sonar & navigation,* 14**,** 431-438. doi: 10.1049/iet-rsn.2019.0500.

[13] Ge, M., Cui, G. & Kong, L. 2019. Mainlobe jamming suppression for distributed radar via joint blind source separation. *IET Radar, Sonar & Navigation,* 13**,** 1189-1199. doi: 10.1049/iet-rsn.2018.5434.

[14] Zhang, X., Cao, D. & Xu, L. 2019. Joint polarisation and frequency diversity for deceptive jamming suppression in MIMO radar. *IET Radar, Sonar & Navigation,* 13**,** 263-271. doi: 10.1049/iet-rsn.2018.5342.

[15] Xiang, Z., Chen, B. & Yang, M. 2018. Transmitter/receiver polarisation optimisation based on oblique projection filtering for mainlobe interference suppression in polarimetric multiple-input–multiple-output radar. *IET Radar, Sonar & Navigation,* 12**,** 137-144. doi: 10.1049/iet-rsn.2016.0648.

[16] Lan, L., Xu, J., Liao, G., Zhang, Y., Fioranelli, F. & So, H. C. 2020. Suppression of mainbeam deceptive jammer with FDA-MIMO radar. *IEEE Transactions on Vehicular Technology,* 69**,** 11584-11598. doi: 10.1109/TVT.2020.3014689.

[17] Xu, J., Liao, G., Zhu, S. & So, H. C. 2015. Deceptive jamming suppression with frequency diverse MIMO radar. Signal Processing, 113, 9-17. doi: 10.1016/j.sigpro.2015.01.014.

[18] Ding, L., Li, R., Dai, L., Chen, F. & Wang, Y. 2017. Discrimination and identification between mainlobe repeater jamming and target echo via sparse recovery. *IET radar, sonar & navigation,* 11**,** 235-242. doi: 10.1049/iet-rsn.2016.0109.

[19] Zhou, B., Duan, K., Liu, W., Li, R. & Wang, Y. 2019. Sparse Bayesian learning-based mainlobe blanket jamming suppression algorithm. *The Journal of Engineering,* 2019**,** 7069-7073. doi: 10.1049/joe.2019.0407.

[20] Cheng, Y., Zhu, D. & Zhang, J. 2020. High precision sparse reconstruction scheme for multiple radar mainlobe jammings. *Electronics,* 9**,** 1224. doi: 10.3390/electronics9081224.

[21] Xin, L., Baoguo, Y. & Ping, H. 2018. Mainlobe interference suppression via eigen-projection processing and covariance matrix sparse reconstruction. *IEICE Electronics Express,* 15**,** 20180683-20180683. doi: 10.1587/elex.15.20180683.

[22] Mohimani, H., Babaie-Zadeh, M. & Jutten, C. 2008. A fast approach for overcomplete sparse decomposition based on smoothed ℓ0 norm. *IEEE Transactions on Signal Processing,* 57**,** 289-301. H. doi: 2008 10.1109/TSP.2008.2007606.

[23] Ghaffari, A., Babaie-Zadeh, M. & Jutten, C. Sparse decomposition of two dimensional signals. 2009 IEEE international conference on acoustics, speech and signal processing, 2009. IEEE, 3157-3160. doi: 10.1109/ICASSP.2009.4960294.

[24] Zhang, D., Zhang, Y. & Feng, C. 2017. Joint-2D-SL0 algorithm for joint sparse matrix reconstruction. *International Journal of Antennas and Propagation,* 2017. doi: 10.1155/2017/6862852.

[25] Bu, H., Tao, R., Bai, X. & Zhao, J. 2016. Regularized smoothed ℓ0 norm algorithm and its application to CS-based radar imaging. *Signal Processing,* 122**,** 115-122. doi: 10.1016/j.sigpro.2015.11.024.

[26] Hu, X., Tong, N., Zhang, Y. & Huang, D. 2018. MIMO radar imaging with nonorthogonal waveforms based on joint-block sparse recovery. *IEEE Transactions on Geoscience and Remote Sensing,* 56**,** 5985-5996. doi: 10.1109/TGRS.2018.2829403.

[27] Chen, J., Zhou, Y., Jin, L., Li, J. & Zhu, Y. 2017. An adaptive regularized smoothed ℓ° norm algorithm for sparse signal recovery in noisy environments. *Signal Processing,* 135**,** 153-157. doi: 10.1016/j.sigpro.2017.01.004 10.1109/TSP.2021.3086362.

[28] Lu, X., Xu, B., Yeo, T. S., Su, W. & Gu, H. 2021. Co-located MIMO radar target detection in cluttered and noisy environment based on 2D block sparse recovery. *IEEE Transactions on Signal Processing,* 69**,** 3431-3445. doi: 10.1109/TSP.2021.3086362.

[29] Sorensen, D. C. & Antoulas, A. 2002. The Sylvester equation and approximate balanced reduction. *Linear algebra and its applications,* 351**,** 671-700. doi: 10.1016/S0024-3795(02)00283-5.

[30] Bartels, R. H. & Stewart, G. W. 1972. Solution of the matrix equation AX+ XB= C [F4]. *Communications of the ACM,* 15**,** 820-826. doi: 10.1145/361573.361582.